Kinetics of the inner ring in the exciton emission pattern in coupled GaAs quantum wells

A. T. Hammack and L. V. Butov

Department of Physics, University of California at San Diego, La Jolla, California 92093-0319, USA

J. Wilkes, L. Mouchliadis, E. A. Muljarov, and A. L. Ivanov

Department of Physics and Astronomy, Cardiff University, Cardiff CF24 3AA, United Kingdom

A. C. Gossard

Materials Department, University of California at Santa Barbara, Santa Barbara, California 93106-5050, USA

We report on the kinetics of the inner ring in the exciton emission pattern. The formation time of the inner ring following the onset of the laser excitation is found to be about 30 ns. The inner ring is also found to disappear within 4 ns after the laser termination. The latter process is accompanied by a jump in the photoluminescence (PL) intensity. The spatial dependence of the PL jump indicates that the excitons outside of the region of laser excitation, including the inner ring region, are efficiently cooled to the lattice temperature even during the laser excitation. The ring formation and disappearance are explained in terms of exciton transport and cooling.

I. INTRODUCTION

An *indirect exciton* is a bound pair of an electron and a hole confined in spatially separated layers. It can be realized in coupled quantum well (CQW) structures. The reduction in the overlap of electron and hole wave functions, when they are separated into neighboring quantum wells, results in a large enhancement of the lifetime of indirect excitons compared to that of regular direct excitons in a single quantum well. This increase in lifetime allows the indirect excitons to travel large distances[1–9] and to cool down to temperatures T well below the onset of quantum degeneracy that occurs at $T \simeq T_{\mathrm{dB}} = (2\pi\hbar^2 n_x)/(M_x g k_B) \simeq 3$ K for the density per spin state $n_x/g = 10^{10}$ cm^{-2} (in the CQWs studied, the exciton translational mass is $M_x \simeq 0.22 m_0$ and the spin degeneracy factor is $g = 4$).[10] Furthermore, the built-in dipole moment of an indirect exciton, ed, allows control of exciton transport by electrode voltages[1,7,11–13] (d is the separation between the electron and hole layers). The combination of long lifetime, large transport distance, efficient cooling, and an ability to control exciton transport makes the indirect excitons a model system for the investigation of in-plane transport of quasi-two-dimensional (quasi-2D) cold Bose gases in solid-state materials.

Studies of indirect excitons in CQWs have lead to the finding of a number of phenomena including exciton pattern formation, a review of which can be found in Ref. 14. The features of the exciton emission pattern include the inner ring,[4,6] external ring,[4,15–19] localized bright spots,[4,16,20–22] and macroscopically ordered exciton state.[4,16,23,24] In the regular excitation scheme, where excitons are generated in a micron scale focused laser-excitation spot, the inner ring forms around the excitation spot. It was discussed in terms of the cooling of indirect excitons during their propagation away from the excitation spot.[4,6] However, to date, measurements of the spatial kinetics of the inner ring were unavailable. In this paper, we present studies of the spatially and spectrally resolved kinetics of the exciton inner ring. The results show

that the exciton inner ring forms and reaches a steady state within the first few tens of nanoseconds of laser excitation, and also disappears within a few nanoseconds after the laser termination. The spatially temporal behavior of the inner ring is modeled in terms of in-plane exciton transport and cooling toward the phonon bath (cryostat) temperature.

In Sec. II, we describe the experimental data and compare them with numerical simulations of the kinetics of the inner ring in the exciton emission pattern. In Sec. III, a model of in-plane transport, thermalization, and photoluminescence (PL) of indirect excitons is presented. In Sec. IV, we discuss the results. A short summary of the work is given in Sec. V.

II. EXPERIMENTAL DATA AND NUMERICAL SIMULATIONS

The measurements were performed using temporal-resolved imaging with 4 ns time resolution and 2 μm spatial resolution. Excitons were photogenerated by a pulsed laser at 635 nm with pulse duration of 500 ns and edge sharpness of <1 ns, operating with a period of 1 μs. The period and duty cycle were chosen such that the PL pattern of indirect excitons was able to reach equilibrium during the laser excitation and to allow for complete decay of the PL of indirect excitons between laser pulses. The laser was focused to a 10 μm full width at half maximum (FWHM) excitation spot on the CQW sample. The excitation density P_{ex} was chosen to be below that at which the external ring appears in the emission pattern.[4] A nitrogen-cooled charge-coupled device camera (CCD) coupled to a PicoStar HR TauTec intensifier with a time-integration window of $\delta t = 4$ ns was used to acquire (E, r) PL images at varied delay time t. The spectral information was captured by placing the time-gated intensifier and CCD after a single grating spectrometer. The spectral diffraction and time-gated imaging combined allow the direct visualization of the evolution of the indirect exciton PL
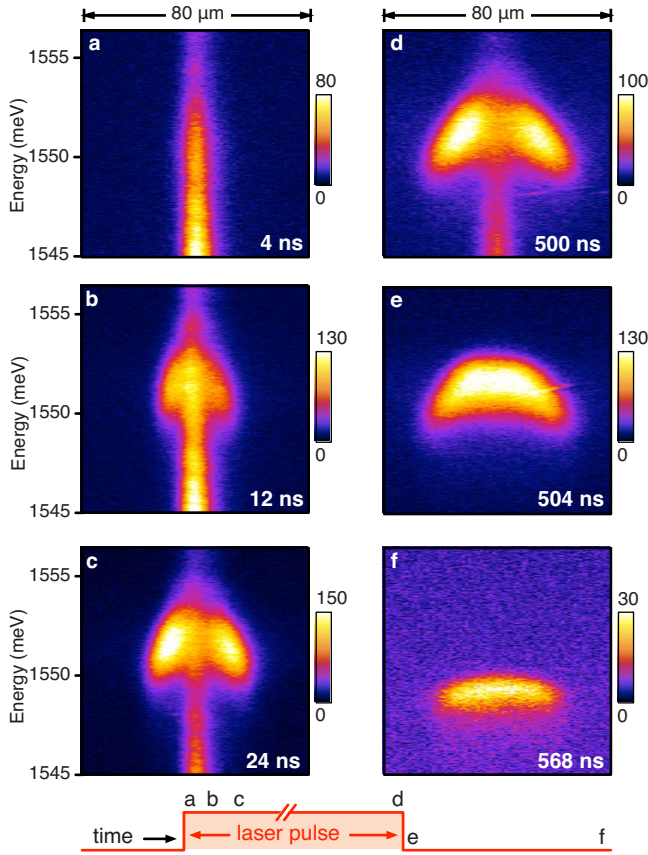
FIG. 1. (Color online) The energy-radius (E, r) images of the exciton energy versus radius during the time evolution of the exciton inner ring following the onset and termination of the rectangular laser pulse. Time $t = 0$ ns corresponds to the onset of the laser pulse of the duration $\tau_{pulse} = 500$ ns. Each image is integrated over a time window of $\delta t = 4$ ns ending at the times [(a)–(c)] $t = 4$, 12, and 24 ns after the start of the laser pulse, and [(d)–(f)] $t - \tau_{pulse} = 0$, 4, and 68 ns after its termination. The laser is focused to a 10 μm full width half maximum (FWHM) excitation spot on the CQW sample.

intensity and energy as a function of delay time t [see Figs. 1(a)–1(c) for the laser onset and Figs. 1(d)–1(f) for the laser termination]. Experiments were performed at the applied gate voltage 1.2 V, peak excitation power 150 μW, and bath temperature 1.4 K.

The CQW structure used in these experiments contains two 8 nm GaAs QWs separated by a 4 nm $Al_{0.33}Ga_{0.67}As$ barrier. The sample was grown by molecular-beam epitaxy (details on the CQW structures can be found in Ref. 4). The effective spacing between the electron and hole layers is given by $d = 11.5$ nm.[25]

Figures 1(a)–1(c) show the emergence in time of an arrow-shaped profile of the indirect exciton PL signal plotted in (E, r) coordinates. The central bright stripe corresponds to the bulk n^+ GaAs emission. The n^+ GaAs layers are separated 200 nm from the CQW and their emission line spreads down to about 1.48 eV. Its spatial profile essentially corresponds to the laser-excitation profile. The emission of indirect excitons is observed at the sides of this stripe beyond the excitation spot, due to the exciton transport. The emission energy drops with increasing distance from the origin r (see
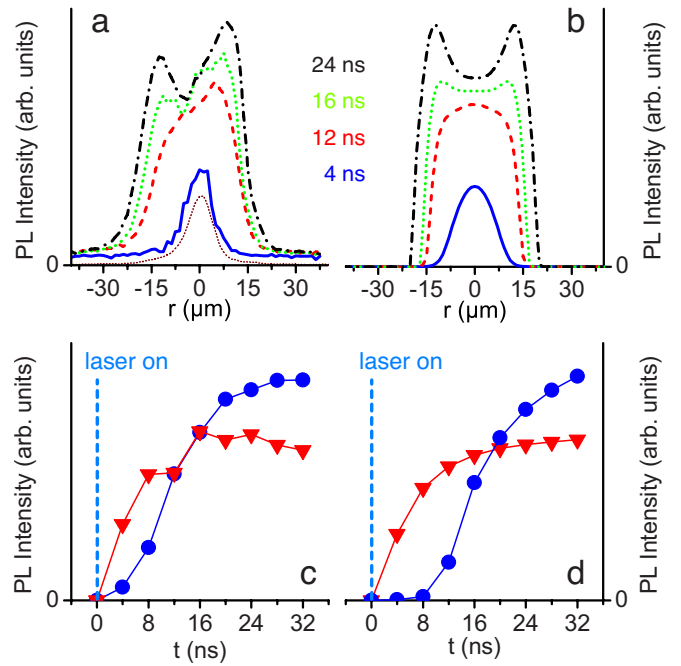

FIG. 2. (Color online) Kinetics of the indirect exciton PL profile after the laser-excitation onset. The (a) measured and (b) calculated cross sections of the indirect exciton PL across the diameter of the inner exciton ring as a function of time. The (c) measured and (d) calculated indirect exciton PL intensity at the center of the laser-excitation spot (red ▼) and at the inner ring radius $r = r_{ring} \simeq 12$ μm (blue ●), where the PL maximum signal occurs, as a function of time. The time-integration window $\delta t = 4$ ns for each profile (a) and (b) and each point (c) and (d). The times $t = 0$ ns and $t = 500$ ns correspond to the onset and termination of the rectangular laser-excitation pulse. The laser-excitation profile is shown by the thin dotted line in (a).

Fig. 1). The drop in energy with increasing r corresponds to a decrease in density, as detailed in Ref. 6 where the inner ring was studied without time resolution. At early times, when the indirect exciton signal is small, the bulk emission, consisting of the central bright stripe, dominates [see Fig. 1(a)]. After sufficient time, the exciton inner ring becomes apparent by the presence of a dip in the PL of indirect excitons within the region of laser excitation at the center of the exciton cloud. It is worth noting that the decrease in the exciton PL does not correspond to a dip in the exciton density, which has its maximum at the center of the laser-excitation spot (see Fig. 1).

The kinetics presented in Figs. 2(a) and 2(c) show the total spectrally integrated PL intensity of indirect excitons taken from a series of time-gated spectrally resolved images. The data shows that the inner ring forms and reaches a steady state within the first few tens of ns of the laser-excitation pulse. Both the spatial and temporal character of the experimental data is in agreement with simulations using a kinetic model for the indirect exciton transport, cooling, and optical decay [see Fig. 2(a) vs Fig. 2(b) and Fig. 2(c) vs Fig. 2(d)]. The model is detailed in Sec. III.

These results demonstrate that within few tens of ns the excitons are able to propagate tens of microns away from the generation region. The large-scale transport is indicative that

excitons are capable to screen effectively the disorder potential intrinsic to the quantum wells, leading to enhanced drift and diffusion.[26] This is consistent with the exciton diffusion coefficient D_x evaluated with the thermionic model and plotted in Fig. 5(d). An increase in D_x at a given radius r with increasing time (increasing exciton density) and a decrease in D_x at a given time t with increasing radius (decreasing density) are seen.

Only excitons from the radiative zone with kinetic energy $E \leq E_\gamma \simeq (E_x^2 \varepsilon_b)/(2mc^2)$ are optically active,[27–29] with E_x the exciton energy and ε_b the background dielectric constant. The excitons traveling away from the excitation spot cool down toward the lattice temperature. This results in the increase in the occupation of the radiative zone, giving rise to an increase in the emission intensity and therefore leading to the formation of the PL ring. The underlying physics is further illustrated in Fig. 5, where numerical simulations of $T = T(t)$, $D_x = D_x(t)$, $n_x = n_x(t)$, and the optical lifetime of indirect excitons, $\tau_{opt} = \tau_{opt}(t)$, are plotted for the onset of the laser excitation.

Upon termination of the laser pulse [see Figs. 1(d)–1(f)], an abrupt increase in the PL intensity is detected at the laser-excitation spot [see Figs. 3(a), 3(c), and 3(e)]. After the laser switches off, the optically dark, high-energy excitons outside the light cone relax to the radiative zone, leading to the observed *PL jump*. Experiments performed without spatial resolution have already revealed the PL jump.[10] However, the results of the time-resolved imaging experiments presented here clarify that the PL jump is observed predominantly within the laser-excitation spot, where indirect excitons are heated by the laser. Within 4 ns, the time resolution of the current experiments, the excitons cool down to the lattice temperature $T_b = 1.4$ K. The characteristic cooling (thermalization) time, as calculated with the model described in Sec. III, is $\tau_{th} \simeq 0.2$ ns [see Fig. 5(a)]. The contrast of the PL jump is defined as $(I_{max} - I_{laser\ on})/I_{laser\ on}$ with $I_{max} = I_{max}(r)$ and $I_{laser\ on} = I_{laser\ on}(r)$ the maximum PL intensity after the laser-pulse termination and the steady-state PL intensity in the presence of the laser pulse, respectively. The measured contrast of the PL jump against the radial distance r is plotted in Fig. 3(c). Averaging the numerical simulations [see inset of Fig. 3(d)] over the 4 ns integration window to match the experimental conditions leads to the PL-jump contrast shown in Fig. 3(d), in agreement with the experiment [see Figs. 3(c) and 3(e) vs Figs. 3(d) and 3(f)].

The monotonic decrease in the PL jump with increasing radius [see Figs. 3(c) and 3(d)] demonstrates that the effective exciton temperature T during the laser excitation lowers with increasing r. This is consistent with the model we use. The numerical simulations of the exciton temperature profile, plotted in the inset of Fig. 6(a) for two time delays, 0 and 4 ns after the termination of the laser pulse, are in agreement with the spatial dependence of the PL jump shown in Fig. 3. Both the experimental data and calculations demonstrate that the exciton cooling time to the lattice temperature is much shorter than the exciton lifetime $\tau_{opt} \simeq 50$ ns.

Both the excitation and emission patterns (a laser-excitation spot and a PL ring around the excitation spot, which develops at large delay times), studied in the present work, correspond to the geometry inverted compared to that
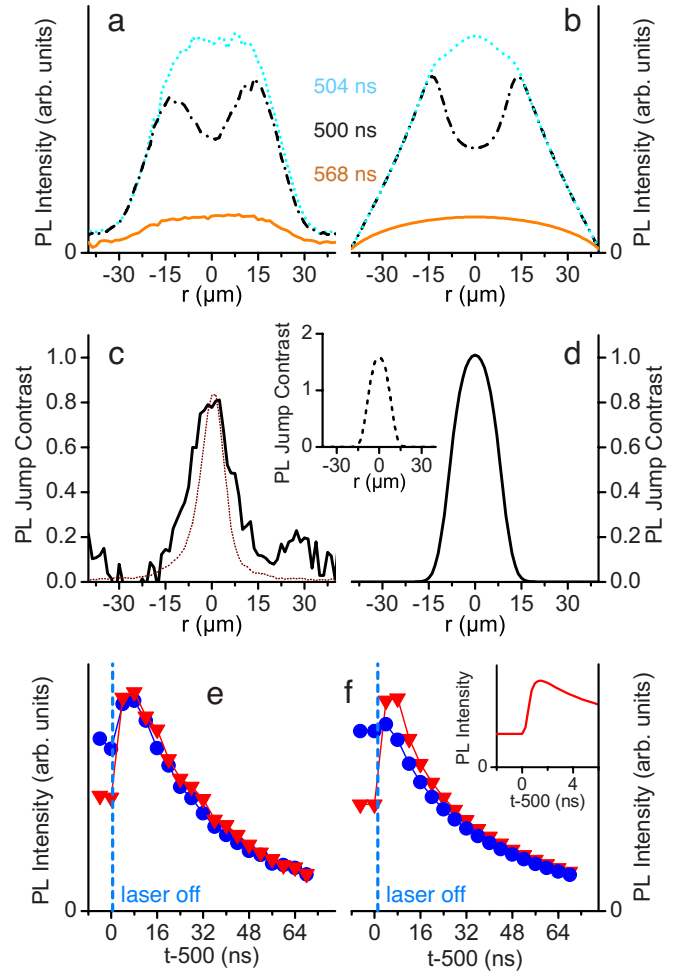

FIG. 3. (Color online) Kinetics of the indirect exciton PL profile during the laser-excitation termination. The (a) measured and (b) calculated with Eqs. (1)–(3) spatial profiles of the PL signal from indirect excitons across the inner ring at the times $t = 500$ ns (dash-dotted line), 504 ns (dotted line), and 568 ns (solid line). The times $t = 0$ ns and $t = 500$ ns correspond to the onset and termination of the rectangular laser-excitation pulse. The (c) measured and (d) evaluated numerically contrast of the PL jump $(I_{max} - I_{laser\ on})/I_{laser\ on}$ against the radial coordinate. The laser-excitation profile is shown by the dotted line in (c). The (e) measured and (f) calculated indirect exciton PL intensity at the center of the laser excitation spot (red ▼) and at the radial distance where the PL maximum intensity occurs, $r = 12$ μm, (blue ●) as a function of time. Insets: (d) The contrast of the PL jump and (f) the PL jump at the center of excitation, evaluated with Eqs. (1)–(3) without time integration to match 4 ns experimental resolution. Apart from the insets, each calculated curve is smoothed by the device resolution function with the time-integration window $\delta t = 4$ ns to match the experimental conditions.

used for the optically induced traps (a ring-shaped laser excitation and a PL pattern concentrated at the center of the excitation ring, which builds up at large delay times).[30] The kinetics of the inner PL ring and the optically induced trap are quantitatively consistent with each other. The most significant distinction between previous works (e.g., Ref. 6) and the results presented here is the detection of PL intensity in the inner ring with both spatial and temporal resolution.

III. MODEL

The set of coupled nonlinear differential equations we use in order to model transport, thermalization, and photoluminescence of indirect excitons is given by

$$\frac{\partial n_x}{\partial t} = \nabla[D_x \nabla n_x + \mu_x n_x \nabla (u_0 n_x + U_{QW})] - \Gamma_{opt} n_x + \Lambda_x, \tag{1}$$

$$\frac{\partial T}{\partial t} = \left(\frac{\partial T}{\partial t}\right)_{n_x} + S_{pump} + S_{opt}, \tag{2}$$

where

$$\left(\frac{\partial T}{\partial t}\right)_{n_x} = -\frac{2\pi}{\tau_{sc}}\left(\frac{T^2}{T_{dB}}\right)(1 - e^{-T_{dB}/T})\int_1^\infty d\varepsilon\varepsilon \sqrt{\frac{\varepsilon}{\varepsilon - 1}}$$
$$\times \frac{|F_z(a\sqrt{\varepsilon(\varepsilon-1)})|^2}{(e^{\varepsilon E_0/k_B T_b} - 1)} \frac{e^{\varepsilon E_0/k_B T_b} - e^{\varepsilon E_0/k_B T}}{(e^{\varepsilon E_0/k_B T} + e^{-T_{dB}/T} - 1)},$$

$$I_{PL}^{sig} = \Gamma_{opt}^{sig} n_x, \tag{2}$$

where

$$\Gamma_{opt}^{sig} = \frac{1}{2\tau_R}\left(\frac{E_\gamma}{k_B T_{dB}}\right)$$
$$\times \int_{z_s}^1 \frac{1 + z^2}{[(e^{E_\gamma/k_B T})/(1 - e^{-T_{dB}/T})]e^{-z^2 E_\gamma/k_B T} - 1} dz. \tag{3}$$

Equations (1)–(3) describe in-plane profiles of the density $n_x = n_x(r,t)$, effective temperature $T = T(r,t)$, and PL signal intensity $I_{PL}^{sig} = I_{PL}^{sig}(r,t)$ of indirect excitons.

In the drift diffusion Eq. (1) for in-plane transport of the particles,[26] D_x, μ_x, Γ_{opt}, and Λ_x are the diffusion coefficient, mobility, radiative decay rate, and generation rate of indirect excitons, respectively. The ∇ operator has only the radial component, $\nabla_r = \partial/\partial r$, due to the cylindrical symmetry one deals with. The mobility μ_x is given in terms of the diffusion coefficient D_x through the generalized Einstein relationship, $\mu_x = D_x[(e^{T_{dB}/T} - 1)/(k_B T_{dB})]$.[26] The random potential $U_{QW} = U_{rand}(\mathbf{r})$ on the right-hand side (rhs) of Eq. (1) is mainly due to the CQWs thickness and alloy fluctuations. The drift term $\propto \nabla(u_0 n_x + U_{QW})$ stems from the dipole-dipole interaction of indirect excitons and the in-plane potential U_{QW}. For the first contribution we use $u_0 = 4\pi d(e^2/\varepsilon_b)$. This stems from the dipole-dipole repulsion between the particles and gives rise to the blueshift of the PL line. For $n_x \gtrsim 10^9 \text{cm}^{-2}$ relevant to the experiment, the correlation energy of exciton-exciton interaction is less than the mean-field energy[31] and therefore is neglected in the present model. The radiative rate $\Gamma_{opt} = 1/\tau_{opt}$ on the rhs of Eq. (1) is $\Gamma_{opt} = \Gamma_{opt}^{sig}(z_s = 0)$ with Γ_{opt}^{sig} given by Eq. (3).

The first term on the rhs of Eq. (2), $(\partial T/\partial t)_{n_x}$, describes thermalization (cooling) of indirect excitons, due to their interaction with a bath of bulk acoustic phonons at temperature T_b.[32] Here, $\tau_{sc} = (\pi^2 \hbar^4 \rho)/(D_{dp}^2 M_x^3 v_{LA})$ is the characteristic scattering time, $E_0 = 2M_x v_{LA}^2$ is the characteristic energy of

the longitudinal-acoustic (LA) phonon-assisted thermalization at low temperatures, v_{LA} is the velocity of long-wavelength LA phonons, ρ is the crystal density, and $D_{dp} = D_c - D_v$ is the deformation potential of exciton—LA-phonon interaction. The form factor $F_z(a\sqrt{\varepsilon(\varepsilon-1)})$ refers to a rigid-wall confinement potential of quantum wells, where $a = (d_{QW}M_x v_{LA})/\hbar$ with d_{QW} the quantum-well thickness and $\varepsilon = E/E_0$ the normalized single-particle kinetic energy of excitons. The terms S_{pump} and S_{opt} on the rhs of Eq. (2), which are detailed in Ref. 33, deal with heating of indirect excitons by the laser pulse and recombination heating or cooling of the particles. The laser-induced heating is given by

$$S_{pump} = \frac{E_{inc} - k_B T I_2}{2k_B T I_1 - k_B T_{dB} I_2}\Lambda_x^{T_{dB}}, \tag{4}$$

where $\Lambda_x^{T_{dB}} = [(\pi\hbar^2)/(2k_B M_x)]\Lambda_x(r,t)$ and $E_{inc} \gg k_B T_b$ is an average kinetic energy of high-energy indirect excitons injected into the CQW structure by means of photocarriers. The latter are generated in the GaAs and AlGaAs layers by the laser pulse. The term S_{opt}, which takes into account a contribution from the "optical evaporation" of low-energy indirect excitons to the total-energy balance,[33] is determined by

$$S_{opt} = \frac{k_B T I_2 \Gamma_{opt} - E_\gamma \Gamma_{opt}^E}{2k_B T I_1 - k_B T_{dB} I_2}T_{dB}. \tag{5}$$

Here, the energy rate Γ_{opt}^E, due to the optical decay, is given by

$$\Gamma_{opt}^E = \frac{1}{2\tau_R}\left(\frac{E_\gamma}{k_B T_{dB}}\right)$$
$$\times \int_0^1 \frac{1 - z^4}{[(e^{E_\gamma/k_B T})/(1 - e^{-T_{dB}/T})]e^{-z^2 E_\gamma/k_B T} - 1} dz. \tag{6}$$

In Eqs. (4) and (5), the parameters $I_{1,2} = I_{1,2}(T_{dB}/T)$ are $I_1 = (1 - e^{-T_{dB}/T})\int_0^\infty dz[z/(e^z + e^{-T_{dB}/T} - 1)]$ and $I_2 = e^{-T_{dB}/T}\int_0^\infty dz[(ze^z)/(e^z + e^{-T_{dB}/T} - 1)^2]$.

Finally, the intensity I_{PL}^{sig} of the PL signal, collected in the normal direction within an aperture angle α (in the experiment, $\alpha \simeq 30°$), is given by Eq. (3). In this case, the lower integration limit in the expression for the decay rate Γ_{opt}^{sig} is $z_s = 1 - \sin^2(\alpha/2)$ [see Eq. (3)]. Both Γ_{opt}^{sig} and Γ_{opt} are inversely proportional to the intrinsic radiative lifetime τ_R of the exciton ground state with zero in-plane momentum.

In order to evaluate the random drift term $\mu_x n_x \nabla(U_{QW})$ on the rhs of the drift diffusion Eq. (1), we implement a thermionic model.[6,26] In this approach, the influence of disorder is approximately taken into account by using the disorder-dependent effective diffusion coefficient,

$$D_x = D_x^{(0)} \exp\left[-\frac{U^{(0)}}{k_B T + u_0 n_x}\right], \tag{7}$$

where $D_x^{(0)}$ is the input diffusion coefficient in the absence of CQW disorder and $U^{(0)}/2 = \langle|U_{rand}(\mathbf{r}) - \langle U_{rand}(\mathbf{r})\rangle|\rangle$ is the amplitude of the disorder potential. Equation (7) describes temperature- and density-dependent screening of the long-range correlated disorder potential $U_{QW} = U_{rand}(\mathbf{r})$ by dipole-

dipole interacting indirect excitons. The vanishing screening at the external edge of the inner PL ring, due to reduced exciton density, leads to a strong suppression of the exciton propagation away from the excitation spot and, as a result, to the sharp contrast of the ring.[6]

There are two main additional features in our present numerical simulations compared to those reported earlier[6] in order to model a steady-state inner PL ring: (i) we have performed high-resolution numerical simulations with Eqs. (1)–(3) in a space-time domain and (ii) in order to mimic more closely the experiment, we model the source term Λ_x of indirect excitons [see the rhs of Eq. (1)] by assuming a generation of incoming indirect excitons, as secondary particles, from laser-induced photocarriers.

In order to express Λ_x via the generation rate $\Lambda^{(0)}$ of free electron-hole pairs, which are photoexcited in the cladding AlGaAs layers and captured by the GaAs CQW structure, we implement the quantum mass action law (QMAL). According to the QMAL, a total number of electron-hole pairs is distributed among the bound (exciton) and unbound states. For quasi-2D indirect excitons, the QMAL reads as[22,34]

$$n_x = -\frac{2M_x k_B T}{\pi \hbar^2} \ln[1 - e^{\epsilon_x/(k_B T)}(e^{T_{dB}^e/T} - 1)(e^{T_{dB}^h/T} - 1)], \tag{8}$$

where ϵ_x is the (indirect) exciton binding energy and the electron (hole) quantum degeneracy temperature is given by $k_B T_{dB}^{e(h)} = [(\pi \hbar^2)/m_{e(h)}]n_{e(h)}$ with $m_{e(h)}$ and $n_{e(h)}$ the electron (hole) mass and concentration, respectively. Equation (8) characterizes a quasiequilibrium balance between n_x and $n_e = n_h$. A typical time τ_{QMAL} needed to quasiequilibrate the system of electrons, holes, and indirect excitons is comparable to that of binding of photoexcited electrons and holes in excitons. The latter is about 10–30 ps for $n_x \simeq 10^{10}$ cm^{-2} and helium temperatures.[35–39] Because τ_{QMAL} is much less than the characteristic times of the thermalization and transport processes, $\tau_{th} \sim 0.1$ ns and $\tau_{diff} \sim 1$ ns, the use of the QMAL is justified. For the case $T_{dB}^{e(h)} \ll T$, relevant to the experiment, Eq. (8) yields

$$\Lambda_x = \Lambda^{(0)} \frac{4 M_x T_{dB}^{1/2}}{(m_e m_h T)^{1/2} e^{-\epsilon_x/(2 k_B T)} + 4 M_x T_{dB}^{1/2}}. \tag{9}$$

Note that in Eq. (9) the degeneracy temperature T_{dB} is proportional to the accumulated density of indirect excitons, $n_x = n_x(r,t)$. According to numerical evaluations of Eq. (9) adapted to the experimental conditions, apart from the first few hundred picoseconds after the onset of the laser excitation, when $T \gtrsim 10$ K and $n_x \lesssim 10^9$ cm^{-2}, one has $n_x \gg n_{e(h)}$, see Fig. 4, and $\Lambda_x \simeq \Lambda^{(0)}$. Formally, this is because in the denominator on the rhs of Eq. (9) the term $(m_e m_h T)^{1/2} e^{-\epsilon_x/(2 k_B T)}$ is much less than $4 M_x T_{dB}^{1/2}$. In this case, injected electron-hole pairs very effectively transfer to the exciton system.

The observed inner PL ring is nearly radially symmetric in space, when taking the center of the excitation spot as the origin, see Fig. 1 in Ref. 6, as well as the supplementary materials in Ref. 46. Thus in numerical simulations with Eqs. (1)–(3), a polar coordinate system is used and the condition
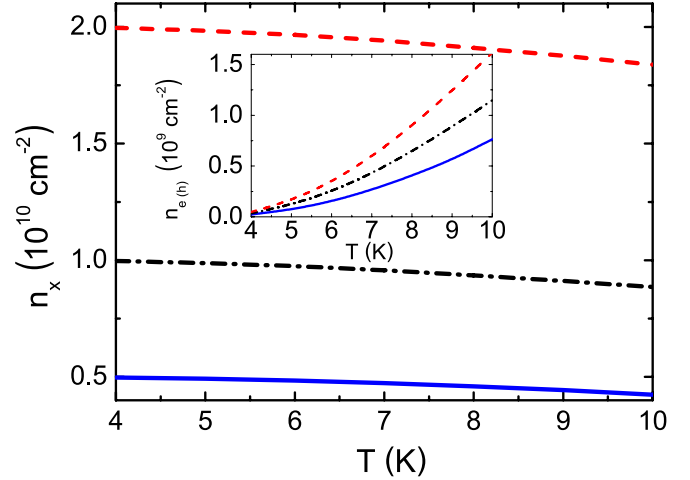

FIG. 4. (Color online) Exciton and electron (hole) concentrations, n_x and $n_e = n_h$, as a function of temperature, evaluated by using the quantum mass action law: $n_x + n_{e(h)} = 2 \times 10^{10}$ cm^{-2} (dashed lines), 10^{10} cm^{-2} (dash-dotted lines), and 0.5×10^{10} cm^{-2} (solid lines). The indirect exciton binding energy $\epsilon_x = 3.5$ meV.

invoked that none of the quantities modeled have any angular dependence. According to the spatial profile of the laser pulse, we assume that the generation rate $\Lambda^{(0)}$ is given by the Gaussian,

$$\Lambda^{(0)} = \Lambda^{(0)}(r,t) = \Lambda^{(0)}(r=0,t)e^{-r^2/r_0^2}, \tag{10}$$

with r_0 the radius of the excitation spot $[r_0 = \text{FWHM}/(2\sqrt{\ln 2}) = 5.8~\mu\text{m}]$. The temporal shape of the rectangular laser pulse with the Gaussian edges is modeled by $\Lambda^{(0)}(r=0,t)$, where $\Lambda^{(0)}(r=0,t) = \widetilde{\Lambda}^{(0)} \exp[-\sigma(t-t_0)^2]$ for $t \leq t_0 = 0.6$ ns, $\widetilde{\Lambda}^{(0)}$ for $t_0 \leq t \leq \tau_{pulse} = 500$ ns, and $\widetilde{\Lambda}^{(0)} \exp[-\sigma(t-\tau_{pulse})^2]$ for $t \geq \tau_{pulse}$, and $\sigma = 15.3$ ns^{-2}.

An explicit finite difference scheme (EFDS) is used to integrate the drift diffusion Eq. (1), the only one differential equation among Eqs. (1)–(3) that includes both derivatives, with respect to t and r. In numerical simulations, the time and radial coordinate steps are chosen to be $\Delta t = 6.25$ ps and $\Delta r = 1~\mu$m, respectively. In this case the dimensionless parameter $D_x \Delta t/(\Delta r)^2$ is about 0.01875, ensuring high stability of the EFDS. The various integrals relevant to Eqs. (2)–(6) are calculated using an adaptive Simpson algorithm. Here, special care is taken to evaluate the integrands correctly in the extreme limits of temperature and density.

In order to clarify further the underlying physics of the inner PL ring, in Figs. 5 and 6 we plot $T = T(t)$, $n_x = n_x(t)$, $\tau_{opt} = \tau_{opt}(t)$, and $D_x = D_x(t)$, modeled for the onset and termination edges of the laser-excitation pulse, respectively. The shown dynamics refer to the center of the excitation spot (solid lines), the radial distance $r = r_{ring}$, where a maximum PL signal occurs (dashed lines), $r = r_{ring}/2$ (dotted lines), and $r = 3r_{ring}/2$ (dash-dotted lines).

For the onset of the laser excitation, Figs. 5(a) and 5(b) illustrate the thermalization kinetics of indirect excitons and gradual building up of the density, respectively. The monotonic decrease in τ_{opt} with time is due to the cooling of indirect excitons [see Fig. 5(c)]. A steady-state value of the op-
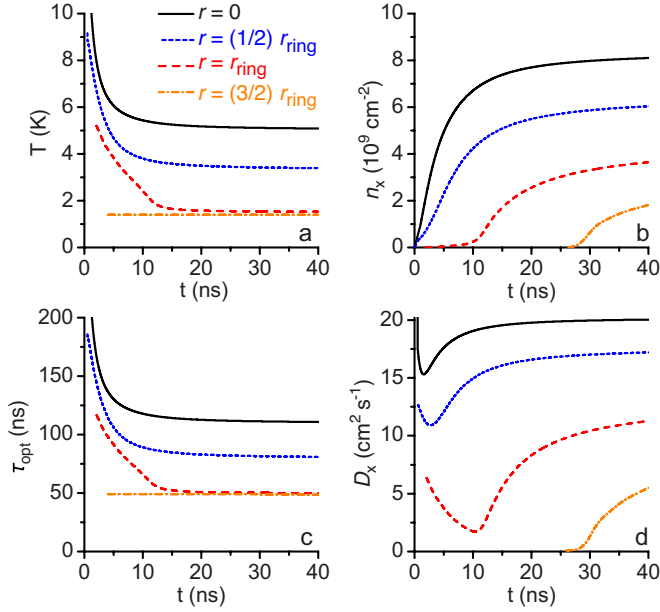
FIG. 5. (Color online) Modeling of the transient dynamics of the (a) exciton temperature T, (b) density n_x, (c) optical lifetime τ_{opt}, and (d) in-plane diffusion coefficient D_x for the onset of the laser excitation. The radial coordinate is $r=0$ (solid line), $r_{ring}/2$ (dotted line), r_{ring} (dashed line), and $3r_{ring}/2$ (dash-dotted line).

tical lifetime decreases with increasing r because the laser-induced heating of the exciton system decreases with the radial distance from the laser spot center. The initial rapid decrease in D_x [see Fig. 5(d)] originates from the thermali-
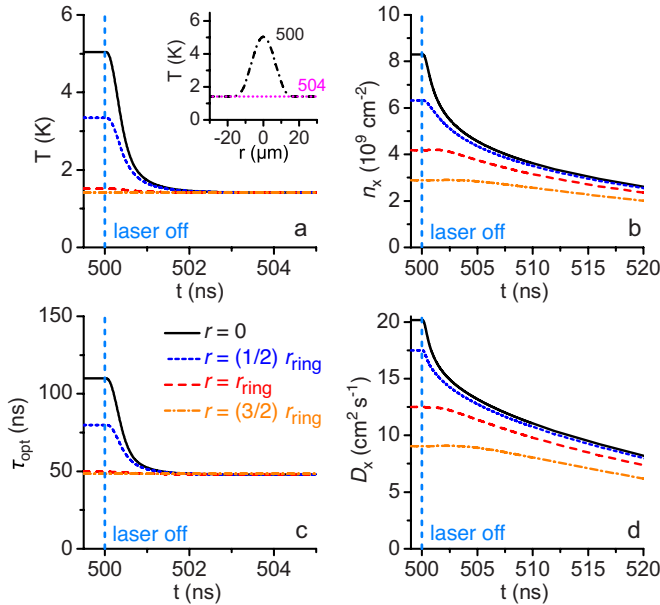

FIG. 6. (Color online) Modeling of the transient dynamics of the (a) exciton temperature T, (b) density n_x, (c) optical lifetime τ_{opt}, and (d) in-plane diffusion coefficient D_x for the termination of the laser excitation. The radial coordinate is $r=0$ (solid line), $r_{ring}/2$ (dotted line), r_{ring} (dashed line), and $3r_{ring}/2$ (dash-dotted line). Inset: The calculated spatial profile of the exciton temperature, $T=T(r)$, for $t=500$ ns (solid line) and $t=504$ ns (dotted line).

zation of the exciton system. Cold excitons cannot overcome the in-plane disorder potential and become localized. A further increase in the diffusion coefficient after the thermalization transient is due to the screening effect which develops with increasing n_x.

For the termination edge of the laser pulse, the decay dynamics shown in Fig. 6 are dominated by the two characteristic times, thermalization time τ_{th} and optical decay time $\tau_{opt} \gg \tau_{th}$. Within the first 1–2 ns, complete thermalization occurs [see Fig. 6(a)], and the system of indirect excitons decays with $\tau_{opt} = \tau_{opt}(T=T_b) \simeq 50$ ns [see Figs. 6(b) and 6(c)]. The gradual decrease in D_x at delay times much larger than τ_{th} [see Fig. 6(d)] is due to the relaxation of the screening effect with decreasing density of indirect excitons.

IV. DISCUSSION

Numerical simulations with Eqs. (1)–(3) quantitatively reproduce the experimental data [see in Figs. 2 and 3 experiment vs modeling] for the following control parameters: $U_0 = 0.7$ meV, $D_x^{(0)} = 30$ cm²/s, $\tilde{\Lambda}^{(0)} = 2 \times 10^9$ cm⁻² ns⁻¹, and $E_{inc} = 12.9$ meV. Although we use four fitting parameters, the procedure is well justified: (i) the whole set of the experimental data, measured at various r and t, are modeled with the same values of the control parameters and (ii) the fitting parameters influence different aspects of the transport and PL processes in a separate way, i.e., can be inferred independently. The pump rate $\tilde{\Lambda}^{(0)}$ yields a maximum concentration $n_x^{max} = n_x(r=0, t=\tau_{pulse})$, which, in turn, can be evaluated from the blueshift of the PL line. The average energy of incoming, hot indirect excitons, E_{inc}, governs the contrast of the PL jump. The input diffusion coefficient $D_x^{(0)}$ determines the time-dependent radius of the inner PL ring. Finally, the amplitude U_0 of the long-range correlated disorder potential is responsible for the spatial pinning of the PL signal at ring edges. Note that the above values of the control parameters are consistent with those used in our previous simulations for the steady-state inner ring[6] and laser-induced traps[30,40] studied for the same CQW structures. Table I lists the basic known parameters as well as the parameters of the model.

The model includes the nonclassical, quantum-statistical effects in the description of the transport, thermalization, and optical decay of indirect excitons, Eqs. (1)–(6), (8), and (9) explicitly depend upon T_{dB}. However, the quantum corrections are rather minor, due to relatively weak laser excitations used in the experiment. The quantum effects are not required for the inner ring or the PL-jump formation. Both are classical phenomena associated with the exciton cooling when they travel away from the excitation spot (in the case of the inner ring) or when the excitation pulse is terminated (in the case of the PL jump). However, the quantum degeneracy effects become essential for the dynamics and contrast of the inner PL ring and PL jump, if smaller bath temperatures or higher excitation powers are used.[6,10,30] For instance, bosonic stimulation of exciton scattering can lead to the enhancement of the exciton scattering rate to the low-energy optically active states with increasing exciton concentration as described in Ref. 10.

TABLE I. List of Parameters.

Basic parameters	
M_x	$0.22 m_0$
τ_{sc}	110 ns
τ_R	20 ns
ν_s	3.7×10^5 cm s^{-1}
ρ	5.3 g cm^{-3}
D_{dp}	8.8 eV
T_b	1.4 K
E_0	34.2 μeV
E_γ	138 μeV
L_z	8 nm
ϵ_x	3.5 meV
Model parameters	
$D_x^{(0)}$	30 cm^2 s^{-1}
U_0	0.7 meV
$\tilde{\Lambda}^{(0)}$	2×10^9 cm^{-2} ns^{-1}
E_{inc}	12.9 meV
u_0	1.6×10^{-10} meV cm^2

Note that a ring in the emission pattern can form both in an exciton system[4,6] and in an electron-hole plasma (EHP).[41] In both cases, ring formation requires a long lifetime of the carriers and efficient cooling as they transport away from the excitation spot. The former allows transport over substantial distances while the latter leads to the increase of the emission intensity. However, the exciton system can be distinguished from EHP by the emission linewidth. For a neutral quasi-2D EHP, the emission linewidth should be about the sum of the electron and hole Fermi energies, $\Delta_{EHP} \simeq k_B T_{dB}^e + k_B T_{dB}^h = \pi \hbar^2 n_{e(h)} (1/m_e + 1/m_h)$, with $n_e = n_h$ the density of electrons

and holes in EHP.[42] The smallest density for EHP is determined by the exciton Mott transition $n_M \sim 1/a_B^2$, which occurs due to the phase-space filling and screening (a_B is the exciton Bohr radius).[43] For the CQW structures studied, $m_e \simeq 0.07 m_0$ and $m_h \simeq 0.15 m_0$,[44] the Bohr radius of the indirect excitons $a_B \simeq 20$ nm (Refs. [45]) and $n_M \sim 1/a_B^2 \sim 2 \times 10^{11}$ cm^{-2} so that the smallest linewidth for the EHP is $\Delta_{EHP}^{min} \simeq \pi \hbar^2 n_M (1/m_e + 1/m_e) \sim 10$ meV. In contrast, the linewidth of exciton emission can be well below this value. It is determined by the homogeneous and inhomogeneous broadening and is typically below 2 meV in the CQW structures for the investigated range of densities.[12] The small emission linewidth $\lesssim 2$ meV, which is characteristic for the inner ring reported in Refs. [4], [6], and [41], and in the present paper, indicates that in all these experiments the inner PL ring forms in an exciton system rather than in EHP. See also the supplementary materials.[46]

V. SUMMARY

In summary, we studied kinetics of the inner ring in the exciton emission pattern. The formation time of the inner ring following the onset of the laser excitation is found to be about 30 ns. The inner ring is also found to disappear within 4 ns after the laser termination. The latter process is accompanied by a jump in the PL intensity. The spatial dependence of the PL jump indicates that the excitons outside of the region of laser excitation, including the inner ring region, are efficiently cooled to the lattice temperature even during the laser excitation. The ring formation and disappearance are explained in terms of exciton transport and cooling.

[1] M. Hagn, A. Zrenner, G. Böhm, and G. Weimann, Appl. Phys. Lett. **67**, 232 (1995).

[2] L. V. Butov and A. I. Filin, Phys. Rev. B **58**, 1980 (1998).

[3] A. V. Larionov, V. B. Timofeev, J. Hvam, and K. Soerensen, JETP **90**, 1093 (2000).

[4] L. V. Butov, A. C. Gossard, and D. S. Chemla, Nature (London) **418**, 751 (2002).

[5] Z. Vörös, R. Balili, D. W. Snoke, L. Pfeiffer, and K. West, Phys. Rev. Lett. **94**, 226401 (2005).

[6] A. L. Ivanov, L. E. Smallwood, A. T. Hammack, Sen Yang, L. V. Butov, and A. C. Gossard, Europhys. Lett. **73**, 920 (2006).

[7] A. Gartner, A. W. Holleitner, J. P. Kotthaus, and D. Schul, Appl. Phys. Lett. **89**, 052108 (2006).

[8] A. Gartner, L. Prechtel, D. Schuh, A. W. Holleitner, and J. P. Kotthaus, Phys. Rev. B **76**, 085304 (2007).

[9] X. P. Vogele, D. Schuh, W. Wegscheider, J. P. Kotthaus, and A. W. Holleitner, Phys. Rev. Lett. **103**, 126402 (2009).

[10] L. V. Butov, A. L. Ivanov, A. Imamoglu, P. B. Littlewood, A. A. Shashkin, V. T. Dolgopolov, K. L. Campman, and A. C. Gossard, Phys. Rev. Lett. **86**, 5608 (2001).

[11] A. A. High, E. E. Novitskaya, L. V. Butov, M. Hanson, and A. C. Gossard, Science **321**, 229 (2008).

[12] A. A. High, A. T. Hammack, L. V. Butov, L. Mouchliadis, A. L. Ivanov, M. Hanson, and A. C. Gossard, Nano Lett. **9**, 2094 (2009).

[13] M. Remeika, J. C. Graves, A. T. Hammack, A. D. Meyertholen, M. M. Fogler, L. V. Butov, M. Hanson, and A. C. Gossard, Phys. Rev. Lett. **102**, 186803 (2009).

[14] L. V. Butov, J. Phys.: Condens. Matter **16**, R1577 (2004).

[15] D. Snoke, S. Denev, Y. Liu, L. Pfeiffer, and K. West, Nature (London) **418**, 754 (2002).

[16] L. V. Butov, L. S. Levitov, A. V. Mintsev, B. D. Simons, A. C. Gossard, and D. S. Chemla, Phys. Rev. Lett. **92**, 117404 (2004).

[17] R. Rapaport, G. Chen, D. Snoke, S. H. Simon, L. Pfeiffer, K. West, Y. Liu, and S. Denev, Phys. Rev. Lett. **92**, 117405 (2004).

[18] G. Chen, R. Rapaport, S. H. Simon, L. Pfeiffer, and K. West, Phys. Rev. B **71**, 041301(R) (2005).

[19] M. Haque, Phys. Rev. E **73**, 066207 (2006).

[20] L. V. Butov, C. W. Lai, A. L. Ivanov, A. C. Gossard, and D. S. Chemla, Nature (London) **417**, 47 (2002).

[21] C. W. Lai, J. Zoch, A. C. Gossard, and D. S. Chemla, Science **303**, 503 (2004).

[22] L. Mouchliadis and A. L. Ivanov, J. Phys.: Condens. Matter **19**, 295215 (2007).

[23] L. S. Levitov, B. D. Simons, and L. V. Butov, Phys. Rev. Lett. **94**, 176404 (2005).

[24] S. Yang, A. T. Hammack, M. M. Fogler, L. V. Butov, and A. C. Gossard, Phys. Rev. Lett. **97**, 187402 (2006).

[25] L. V. Butov, A. A. Shashkin, V. T. Dolgopolov, K. L. Campman, and A. C. Gossard, Phys. Rev. B **60**, 8753 (1999).

[26] A. L. Ivanov, Europhys. Lett. **59**, 586 (2002).

[27] J. Feldmann, G. Peter, E. O. Gobel, P. Dawson, K. Moore, C. Foxon, and R. J. Elliott, Phys. Rev. Lett. **59**, 2337 (1987).

[28] E. Hanamura, Phys. Rev. B **38**, 1228 (1988).

[29] L. C. Andreani, F. Tassone, and F. Bassani, Solid State Commun. **77**, 641 (1991).

[30] A. T. Hammack, M. Griswold, L. V. Butov, L. E. Smallwood, A. L. Ivanov, and A. C. Gossard, Phys. Rev. Lett. **96**, 227402 (2006).

[31] A. L. Ivanov, E. A. Muljarov, L. Mouchliadis, and R. Zimmermann, arXiv:0909.4265v1 (unpublished).

[32] A. L. Ivanov, P. B. Littlewood, and H. Haug, Phys. Rev. B **59**, 5032 (1999).

[33] A. L. Ivanov, J. Phys.: Condens. Matter **16**, S3629 (2004).

[34] H. Reinholz, Solid State Commun. **123**, 489 (2002).

[35] T. C. Damen, J. Shah, D. Y. Oberli, D. S. Chemla, J. E. Cunningham, and J. M. Kuo, Phys. Rev. B **42**, 7434 (1990).

[36] R. Strobel, R. Eccleston, J. Kuhl, and K. Köhler, Phys. Rev. B **43**, 12564 (1991).

[37] P. W. M. Blom, P. J. van Hall, C. Smit, J. P. Cuypers, and J. H. Wolter, Phys. Rev. Lett. **71**, 3878 (1993).

[38] M. Gulia, F. Rossi, E. Molinari, P. E. Selbmann, and P. Lugli, Phys. Rev. B **55**, R16049 (1997).

[39] J. Szczytko, L. Kappei, J. Berney, F. Morier-Genoud, M. T. Portella-Oberli, and B. Deveaud, Phys. Rev. Lett. **93**, 137401 (2004).

[40] A. T. Hammack, L. V. Butov, L. Mouchliadis, A. L. Ivanov, and A. C. Gossard, Phys. Rev. B **76**, 193308 (2007).

[41] M. Stern, V. Garmider, E. Segre, M. Rappaport, V. Umansky, Y. Levinson, and I. Bar-Joseph, Phys. Rev. Lett. **101**, 257402 (2008).

[42] L. V. Butov, V. D. Kulakovskii, E. Lach, A. Forchel, and D. Grutzmacher, Phys. Rev. B **44**, 10680 (1991).

[43] S. Schmitt-Rink, D. S. Chemla, and D. A. B. Miller, Adv. Phys. **38**, 89 (1989).

[44] Yu. E. Lozovik, I. V. Ovchinnikov, S. Yu. Volkov, L. V. Butov, and D. S. Chemla, Phys. Rev. B **65**, 235304 (2002).

[45] M. M. Dignam and J. E. Sipe, Phys. Rev. B **43**, 4084 (1991).

[46] See EPAPS Document No. E-PRBMDO-80-101939 for movies showing the measured kinetics of the spatially resolved emission spectra and the simulated kinetics of the spatially resolved PL intensity from the indirect exciton cloud. For the movies of the measured kinetics, the time for each frame is 4 ns and the total durations comprise the 32 ns immediately following the laser onset and 68 ns beginning immediately before the laser termination. The movie of the simulated kinetics shows the full course of the laser-pulse onset and termination. For more information on EPAPS, see http://www.aip.org/pubservs/epaps.html.